Wavelength-scale microdisks as optical gyroscopes: a finite-difference time-domain simulation study

Raktim Sarma, Heeso Noh, and Hui Cao*

Department of Applied Physics, Yale University, New Haven, Connecticut 06520, USA
**Corresponding author: hui.cao@yale.edu*

Received April 13, 2012; accepted May 10, 2012;
posted May 21, 2012 (Doc. ID 166626); published June 14, 2012

We have developed a finite-difference time-domain algorithm to simulate a wavelength-scale optical gyroscope based on a circular microdisk. In addition to the frequency shift, the rotation-induced changes in the quality factor and far-field emission pattern of the whispering gallery modes are studied. Compared to the closed cavity of same size and shape, an open cavity displays a larger frequency splitting by rotation, due to an increase of the mode size. When the disk dimension is on the order of the optical wavelength, the relative change in quality factor by rotation is over an order of magnitude larger than that in resonant frequency, due to enhanced evanescent tunneling of light. These results point to multiple methods for rotation sensing, monitoring the lasing threshold and the output power or the far-field emission pattern of a rotating microdisk laser, which can be much more sensitive than the Sagnac effect in ultrasmall optical gyroscopes.

OCIS codes: 120.5790, 000.4430, 060.2800, 140.3370, 140.4780.

1. INTRODUCTION

Optical gyroscopes have been widely used in industrial and military applications ranging from inertial navigation systems in aircrafts and vessels to control, stabilization, and positioning systems for robotics and virtual reality applications [1]. Compared to the mechanical gyros, optical gyros have higher sensitivity and lower drift rates. All optical rotation sensors exploit the Sagnac effect—the phase difference between two counter-propagating waves along a closed-loop fiber or waveguide. Recently slow light structures, e.g., photonic crystals [2,3] and coupled microresonators [4–8], have been explored for the realization of high-sensitivity miniaturized optical gyroscopes. In addition to the phase shift, a rotation-induced photonic bandgap has been suggested and studied [9]. All these optical gyros are passive in the sense that the light sources are external. The active gyros produce the two counter-propagating beams within the structures, and their frequency difference is often used as a measure of the rotation speed. Microcavity lasers have recently been investigated for ultrasmall active optical gyroscopes [10–13]. Wavelength-scale microdisk cavities have small footprints and can be made with current semiconductor fabrication technologies [10–12]. In addition to the frequency shift, the rotation also modifies the lasing thresholds and the output power levels. Such modifications are caused by the changes of the cavity quality (Q) factors, which can be more sensitive to the rotation than the lasing frequencies [13]. For example, in circular Bragg microlasers, the rotation-induced intensity modulation has exponential dependence on the rotation velocity. In comparison, the Q factors of microdisk cavities are expected to have much less sensitivity to the rotation, because light is confined by total internal reflection (TIR) at the disk boundary. However, as the cavity size approaches the optical wavelength, light leakage through evanescent wave tunneling becomes significant, which could enhance the sensitivity of cavity Q to the rotation.

In the theoretical investigations of optical gyroscopes, diverse strategies have been undertaken, e.g., the direct modal analysis of time-dependent Maxwell's equations in the laboratory frame [14,15], the extension of tight-binding theory to electrodynamics of a rotating medium [2], and the two-dimensional Green's function in a rotating environment [16]. The numerical approaches include the extended transfer matrix method [5] and the finite-difference time-domain (FDTD) algorithm in a rotating frame [17]. The FDTD method is an ab initio, time domain method that can simulate both steady state and transient processes. Analytical results are often difficult to be obtained for complex photonic structures with open boundaries, and the FDTD simulation provides a vital tool for the design and optimization of rotation sensors. An extensive and detailed analysis of the numerical dispersion, the dielectric boundary condition and the perfectly matched layer absorbing boundary conditions in the rotating FDTD model has been performed previously [17].

In this paper, we modify the standard FDTD algorithm for stationary frame to rotating frame by incorporating the modified constitutive relations due to rotation, and simulate a wavelength-scale optical gyroscope based on a circular microdisk. Different from the previous FDTD model, which calculates only E and H, we calculate E, H, D, and B by solving simultaneously and separately the Maxwell's equations and the constitutive relations in the rotating frame. In addition to the frequency shift, we calculate the rotation-induced changes in the Q factors and far-field emission patterns of the whispering gallery (WG) modes. Compared to the closed cavity of same size and shape, an open cavity displays a larger frequency splitting by rotation. This is attributed to larger mode size when the cavity boundary is open. When the cavity size is on the order of the optical wavelength, the rotation-induced change in the Q factor exceeds that of the resonant frequency. This result demonstrates that the WG modes formed by TIR can be sensitive to rotation in ultrasmall

cavities. Moreover, the far-field emission patterns also change dramatically by the rotation. These results point to multiple ways of detecting rotation.

This paper is organized as follows. Section 2 describes the modified FDTD algorithm that we developed to simulate a microcavity under rotation. In Section 3, we validate our FDTD codes by comparing the simulated frequency splitting of WG modes to the analytical results. Section 4 presents the numerical results for the changes in Q factors and far-field patterns of WG modes of rotating microdisks. In Section 4, we also present and compare the frequency splitting and changes in Q factors due to rotation for microdisks of different indices of refraction. Finally we conclude in Section 5.

2. FDTD ALGORITHM FOR ROTATING FRAME

Basic physical laws governing electromagnetic fields are invariant under coordinate transformation including noninertial ones [17,18]. Maxwell's equations therefore retain their form, and the transformation from the stationary frame to a rotating frame is manifested by the changes in the constitutive relations. Assume the medium rotates slowly with a constant angular velocity Ω around a fixed axis, such that $|\Omega L \ll c|$, where L is the maximum distance from the rotation axis, and c is the velocity of light in vacuum. The relativistic effects are therefore negligible, and the constitutive relations in the rotating frame to the first order of Ω are [13,17,18]

$$\varepsilon\vec{E} = \vec{D} + c^{-2}\vec{\Omega}\times\vec{r}\times\vec{H}, \tag{1}$$

$$\mu\vec{H} = \vec{B} - c^{-2}\vec{\Omega}\times\vec{r}\times\vec{E}. \tag{2}$$

We consider a dielectric disk of radius R in free space. The disk is in the xy plane and rotates around its center with $\vec{\Omega} = \Omega\hat{z}$. The disk can be considered as a two-dimensional system with an effective index of refraction n. It has been shown that in a rotating two-dimensional system the electromagnetic fields can be decomposed into transverse electric (TE) and transverse magnetic (TM) modes [16]. Without loss of generality, we concentrate on the TM modes in this paper. For TM modes, the non-vanishing field components are E_z, D_z, H_x, H_y, B_x, and B_y, and the constitutive relations are reduced to

$$\varepsilon E_z = D_z - c^{-2}(\Omega y H_y + \Omega x H_x), \tag{3}$$

$$\mu H_x = B_x - c^{-2}(\Omega x E_z), \tag{4}$$

$$\mu H_y = B_y - c^{-2}(\Omega y E_z). \tag{5}$$

The Maxwell's equations remain the same in the rotating frame, and there are no free charges or currents in the microdisk systems. We adopt the Yee lattice and leapfrog scheme in our FDTD algorithm. All field components are updated with the Maxwell's equations and the constitutive relations in a particular order:

$$\frac{\partial D_z}{\partial t} = \frac{\partial H_y}{\partial x} - \frac{\partial H_x}{\partial y}, \tag{6}$$

$$\varepsilon E_z = D_z - c^{-2}(\Omega y H_y + \Omega x H_x), \tag{7}$$

$$\frac{\partial B_x}{\partial t} = \frac{\partial E_z}{\partial y}, \tag{8}$$

$$\frac{\partial B_y}{\partial t} = \frac{\partial E_z}{\partial x}, \tag{9}$$

$$\mu H_x = B_x - c^{-2}(\Omega x E_z), \tag{10}$$

$$\mu H_y = B_y - c^{-2}(\Omega y E_z). \tag{11}$$

Equations (6), (8), and (9) are identical to those in the stationary frame, and we discretize them in space and time following the standard procedure of Yee's algorithm for a stationary frame. Equations (6), (8), and (9) update D_z, B_x, and B_y, respectively. Equations (7), (10), and (11), which update E_z, H_x, and H_y, respectively, contain additional terms from rotation, which make the discretization complicated.

For example, the discretized form of Eq. (7) in terms of Yee's notation where time step is given by superscript and spatial stepping is given by subscript is

$$\begin{aligned}\varepsilon_{i-1/2,j+1/2}E_z|^n_{i-1/2,j+1/2} = {} & D_z|^n_{i-1/2,j+1/2} \\ & - c^{-2}\Big(\Omega y H_y|^n_{i-1/2,j+1/2} \\ & + \Omega x H_x|^n_{i-1/2,j+1/2}\Big).\end{aligned} \tag{12}$$

The semi-implicit-approximation or temporal average of E_z gives [19]

$$\begin{aligned}\varepsilon_{i-1/2,j+1/2}E_z|^n_{i-1/2,j+1/2} = {} & \varepsilon_{i-1/2,j+1/2}\Big(E_z|^{n+1/2}_{i-1/2,j+1/2} \\ & + E_z|^{n-1/2}_{i-1/2,j+1/2}\Big)/2.\end{aligned}$$

and a similar expression for D_z. The leapfrog scheme does not calculate the value of H_y at $(i-1/2, j+1/2)$, and we therefore use a spatial average as an approximation

$$H_y|^n_{i-1/2,j+1/2} = \Big(H_y|^n_{i-1,j+1/2} + H_y|^n_{i,j+1/2}\Big)/2.$$

Similar spatial average is applied to H_x. After substituting these expressions into Eq. (12) we get

$$\begin{aligned}\varepsilon_{i-1/2,j+1/2}E_z|^{n+1/2}_{i-1/2,j+1/2} = {} & -\varepsilon_{i-1/2,j+1/2}E_z|^{n-1/2}_{i-1/2,j+1/2} \\ & + \Big(D_z|^{n+1/2}_{i-1/2,j+1/2} + D_z|^{n-1/2}_{i-1/2,j+1/2}\Big) \\ & - c^{-2}\Big(\Omega y\Big(H_y|^n_{i-1,j+1/2} + H_y|^n_{i,j+1/2}\Big) \\ & + \Omega x\Big(H_x|^n_{i-1/2,j+1} + H_x|^n_{i-1/2,j}\Big)\Big).\end{aligned} \tag{13}$$

Equation (13) is the final form that we use in our algorithm to update E_z. To update H_x and H_y with Eqs. (10) and (11), we follow the same procedure, but use the semi-implicit approximation or temporal averaging for H_x and H_y, and perform the spatial averaging for E_z:

$$\mu_{i-1/2,j+1}H_x|^{n+1}_{i-1/2,j+1} = -\mu_{i-1/2,j+1}H_x|^{n}_{i-1/2,j+1} + \left(B_x|^{n+1}_{i-1/2,j+1} + B_x|^{n}_{i-1/2,j+1}\right) - c^{-2}\left(\Omega x\left(E_z|^{n+1/2}_{i-1/2,j+1/2} + E_z|^{n+1/2}_{i-1/2,j+3/2}\right)\right), \tag{14}$$

$$\mu_{i,j+1/2}H_y|^{n+1}_{i,j+1/2} = -\mu_{i,j+1/2}H_y|^{n}_{i,j+1/2} + \left(B_y|^{n+1}_{i,j+1/2} + B_y|^{n}_{i,j+1/2}\right) - c^{-2}\left(\Omega y\left(E_z|^{n+1/2}_{i+1/2,j+1/2} + E_z|^{n+1/2}_{i-1/2,j+1/2}\right)\right). \tag{15}$$

Our algorithm therefore uses Maxwell's equations to update D and B from E and H, and the constitutive relations to update E and H from D and B. Although it includes additional quantities and equations compared to the previous FDTD algorithm, our algorithm is actually simpler as there are no time derivates or spatial derivatives in the extra equations. This may improve the numerical stability and accuracy of the FDTD simulation.

For simulating a stationary or rotating closed cavity, we use Dirichlet Boundary conditions in our FDTD algorithm. For stationary or rotating open cavities, we terminate the main grid by a uniaxial perfectly matched layer (UPML) designed for a stationary frame. The condition for vanishing reflection from the UPML has been obtained in the stationary frame [19]. In a rotating frame, since the constitutive relations are changed, the zero reflection condition cannot be perfectly satisfied [17]. To determine the applicability of the UPML designed for a stationary frame in a rotating frame, we estimate the error caused by residual reflection from the UPML. The test region and benchmark region share the center, and both have a square-shaped main grid terminated by UPML. However the main grid of the benchmark region is five times bigger than that of the test region. We launch a hard source at the centre of both the test region and the benchmark region at the initial time step $n = 0$, and calculate the global error [19]

$$e_{\text{global}}|^n = \sum_i \sum_j |E_{z,T}|^n_{i,j} - E_{z,B}|^n_{i,j}|^2 \tag{16}$$

at various time steps n, where $E_{z,T}|^n_{i,j}$ is the value of E_z at time step n and position (i,j) in the test region and $E_{z,B}|^n_{i,j}$ is in the benchmark region. After the source has propagated and reached the UPML of the test region but not the UPML of the benchmark region, Eq. (16) gives an estimation of the reflection from the UPML.

We observed, for a stationary main grid terminated by a stationary UPML, the maximum global error is $\sim 1.3 \times 10^{-12}$. For a rotating main grid with the maximum $v/c \sim 0.01$ and terminated by stationary UPML, the maximum global error is $\sim 2.1 \times 10^{-6}$. The global error increases by a factor of $\sim 10^6$ but still is small enough and the reflection does not corrupt the results as shown in the next section.

3. SAGNAC EFFECT IN A MICRODISK CAVITY

In this section, we test our FDTD code by comparing the frequency shift in a rotating microdisk to the analytical result. In the rotating frame, the wave equation for electric field of TM polarized light can be written in the polar coordinates as [10,12,13]

$$\left[\frac{\partial^2}{\partial r^2} + \left(\frac{1}{r}\right)\left(\frac{\partial}{\partial r}\right) + \frac{1}{r^2}\frac{\partial^2}{\partial \theta^2} + 2ik\frac{\Omega}{c}\frac{\partial}{\partial \theta} + n^2k^2\right]E_z = 0. \tag{17}$$

In a circular disk, $E_z(r,\theta) = f(r)\exp(-im\theta)$, where m is an integer, and

$$\left[\frac{\partial^2}{\partial r^2} + \left(\frac{1}{r}\right)\left(\frac{\partial}{\partial r}\right) - \frac{m^2}{r^2} + K_m^2\right]f(r) = 0, \tag{18}$$

where

$$K_m^2 = k^2\left[n^2 + 2m\left(\frac{\Omega}{\omega}\right)\right]. \tag{19}$$

Equation (19) implies that rotation induces a change in the dielectric constant or the refractive index, which is given by $n_{\text{eff}}^2 = n^2 + 2m(\Omega/\omega)$ [13]. For a given direction of rotation, the clockwise (CW) and counterclockwise (CCW) waves inside the cavity experience different n_{eff} as they have opposite signs of the azimuthal number, m. The wave traveling in the same direction of rotation acquires a higher n_{eff} than that traveling in the opposite rotation. Thus rotation lifts the degeneracy of WG modes. For a closed cavity, where Dirichlet Boundary conditions are applied at the boundary, the frequency splitting between the CW and CCW modes can be obtained analytically to the first order of Ω [10]:

$$\Delta\omega = 2(m/n^2)\Omega. \tag{20}$$

Equation (20) corresponds to the Sagnac effect in a closed cavity. For an open cavity, n_{eff} is modified both inside and outside the cavity.

Using our FDTD algorithm, we simulate a rotating microdisk cavity with both closed and open boundary. The circular disk has a radius $R = 590$ nm and a refractive index $n_0^{\text{disk}} = 3$. In order to find the frequencies of resonant modes in a stationary open cavity, we first launch a seed pulse with a broad bandwidth centered at $\lambda = 2R$ to excite many cavity resonances. The modes with shorter lifetime will decay faster in time, and the Fourier transform of the field inside the cavity at a later time will give the frequencies of the surviving modes with longer lifetime. We investigate the mode at $\lambda = 1131.48$ nm with radial number $l = 1$ and azimuthal number $m = 7$. The wavelength of the same mode in the closed cavity can be found from the zero of Bessel Function, which gives $\lambda = 1009.8$ nm. Once we get the resonant frequencies of the stationary cavities, for our simulations of rotating open and closed cavities, we excite only that particular mode by launching a seed pulse with bandwidth narrower than the frequency

spacing between the adjacent modes. The rotation induces a frequency splitting of the CW and CCW modes, which causes a temporal beating of the fields. The Fourier transform of the intracavity electric field give the frequencies of the two split modes. The frequency difference $\Delta\omega$ for the WG modes with $m = \pm 7, l = 1$ in a closed cavity of $R = 590$ nm and $n_0^{\text{disk}} = 3$ is plotted by the circles in Fig. 1, and the solid line is the analytical result from Eq. (20). Their excellent agreement validates our FDTD model.

To test the applicability of the UPML to the rotating case, we simulate a rotating dielectric cavity of $R = 590$ nm and $n_0^{\text{disk}} = 3$ in free space, and calculate the frequency splitting $\Delta\omega$ for the WG modes with $m = \pm 7$ and $l = 1$ (squares in Fig. 1). The effect of rotation can also be treated as a change of the refractive index. According to Eq. (19), the effective index of refraction as a function of the rotation velocity Ω is $(n_\Omega^{\text{disk}})^2 = (n_0^{\text{disk}})^2 + 2m(\Omega/\omega)$, which for $\Omega/\omega \ll 1$ gives $n_\Omega^{\text{disk}} \approx n_0^{\text{disk}} + (m\Omega/n_0^{\text{disk}}\omega)$, where n_Ω^{disk} and n_o^{disk} are the refractive indices for the stationary disk and rotating disk, respectively. Along with the disk, we also change the refractive index outside the cavity in a similar way. The rotation-induced change of the resonant frequency can be calculated with an index change in the stationary case. The frequency splitting calculated in this way for the WG modes of $m = \pm 7$ and $l = 1$ is plotted by the dotted line in Fig. 1, and it agrees well to the FDTD simulation in the rotating frame. Such agreement indicates the residual reflection from the UPML has negligible effect.

Figure 1 shows that an open cavity has a larger frequency splitting between the CW and CCW modes than a closed cavity. It is attributed to the increased mode size in the open cavity. To calculate the spatial distribution of electric field $E_z(x, y)$ for the CW or CCW mode, we use a seed pulse of bandwidth less than the frequency splitting so that only one of the two modes is excited in the FDTD simulation.

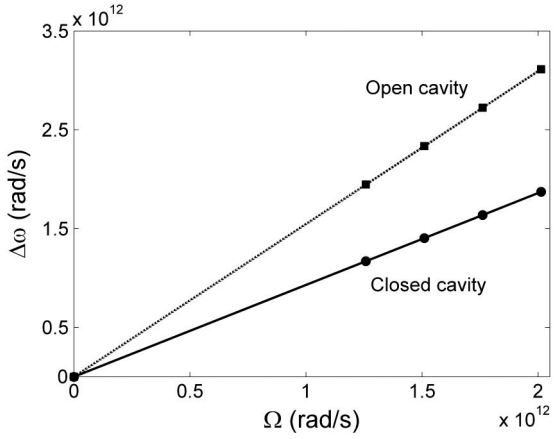

Fig. 1. Frequency splitting between the CW and CCW modes in a circular dielectric microdisk of radius $R = 590$ nm and $n = 3$ in free space ($n = 1$) as a function of the rotation speed Ω. The circles are the FDTD simulation results for a rotating closed cavity for a WG mode ($l = 1, m = 7, \lambda = 1009.8$ nm) and the solid line is the analytical result from Eq. (20). Squares are the FDTD simulation results for the same mode ($l = 1$, $m = 7$, $\lambda = 1131.48$ nm) in the rotating microdisk with open boundary. Dotted line represents the frequency shifts obtained from the FDTD simulation of the stationary microdisk with the effective indices of refraction (inside and outside the disk) that include the rotation-induced changes.

The mode size s is defined as the inverse of the inverse participation ratio (IPF),

$$s = \frac{\left(\iint |E_z(x,y)|^2 \mathrm{d}x\mathrm{d}y\right)^2}{A\left(\int |E_z(x,y)|^4 \mathrm{d}x\mathrm{d}y\right)}, \tag{21}$$

where A is the area of the structure. A mode uniformly distributed over the structure has $s = 1$. A smaller value for s implies that the mode is spatially confined. Figure 2 compares the size of the same mode in the open and closed cavities. The mode size is larger in the open cavity, because the field can extend beyond the disk edge. However, there is not any noticeable change in the mode size as the rotation angular speed increases from 0 to 5×10^{12} rad/s.

4. ROTATION-INDUCED CHANGES IN QUALITY FACTOR AND FAR-FIELD EMISSION PATTERN

In an open cavity, rotation also changes the quality factor of a resonant mode, because the contrast of refractive index inside and outside the disk varies with the rotation and affects the degree of optical confinement by the cavity. For a rotating dielectric microdisk, the refractive index changes both inside and outside the disk, and the refractive index difference is given by

$$n_\Omega^{\text{disk}} - n_\Omega^{\text{outside}} \approx (n_0^{\text{disk}} - n_0^{\text{outside}}) + \left(\frac{m\Omega}{\omega}\right)\left[\frac{1}{n_o^{\text{disk}}} - \frac{1}{n_o^{\text{outside}}}\right]. \tag{22}$$

Equation (22) simplifies for the case of a disk in free space $n_0^{\text{outside}} = 1$ as

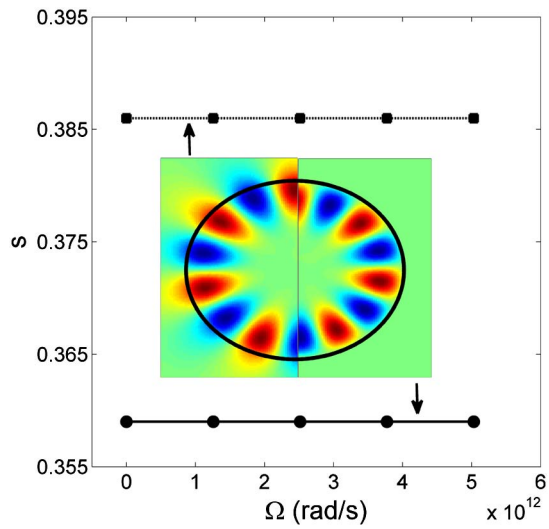

Fig. 2. (Color online) Mode size s as a function of rotation speed Ω. The circles (connected by solid line) are for the mode ($l = 1$, $m = 7$, $\lambda = 1009.8$ nm) in a closed cavity of $R = 590$ nm and $n = 3$ in free space. The squares (connected by dotted line) are for the same mode ($l = 1, m = 7, \lambda = 1131.48$ nm) in the open cavity. The inset shows the electric field distribution of this mode in the open cavity (left half circle) and the closed cavity (right half circle).

$$n_{\Omega}^{\text{disk}} - n_{\Omega}^{\text{outside}} \approx (n_0^{\text{disk}} - 1) + \left(\frac{m\Omega}{\omega}\right)\left[\frac{1}{n_o^{\text{disk}}} - 1\right]. \quad (23)$$

Equation (23) implies the rotation increases the refractive index difference for negative m. Thus the Q factor for the counter-propagating mode increases with the rotation speed Ω. For the co-propagating mode with positive m, the Q factor decreases with rotation. In the case of a microdisk, the change in the refractive index contrast is symmetric and opposite for the CW and CCW modes. Figure 3 plots the Q values obtained from the simulation (given by the squares) for the WG modes of $l = 1$ and $m = \pm 7$ for the same open cavity ($R = 590$ nm, $n_0^{\text{disk}} = 3$) as in Fig. 1 versus Ω. For the $m = 7$ mode, we see a decrease in the Q factor whereas the Q factor for the $m = -7$ mode increases. The change has the same magnitude but opposite sign for the two modes. Within the range of rotation speed in the simulation, we observe an exponential dependence of $\Delta Q = Q_{\text{CW}}(\Omega) - Q_{\text{CW}}(\Omega = 0)$ on Ω. This is because $\Omega/\omega \ll 1$ and the rotation-induced change of the refractive index scales linearly with Ω. The Q factor of a TIR-based WG mode depends exponentially on the difference in the refractive index inside and outside the disk, which scales linearly with the rotation speed according to Eq. (22).

In the simulation, the Q factor of a cavity mode is extracted from the temporal decay of the field. At a given rotation speed, a single mode at frequency ω is excited by a seed pulse launched near the disk edge. By making the bandwidth of the pulse narrower than the frequency difference between the CW and CCW modes, we ensure only one mode is excited and eliminate beating in the time trace of E_z. $E_z(t)$ displays an exponential decay after the seed pulse is gone, and from the decay time τ we obtain $Q = \omega\tau$, where $\omega$is the resonant frequency.

An important point to notice is that, for this wavelength-scale cavity we are studying, the sensitivity of the Q factor to rotation is more than one order of magnitude higher compared to the change in frequency. Figure 4 plots the relative change in Q, $\Delta Q/Q_0$, as a function of Ω, in comparison with

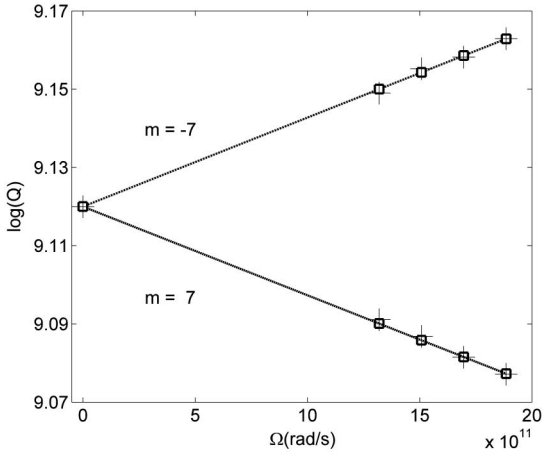

Fig. 3. Calculated quality factors for the $l = 1$, $m = \pm 7$ modes as a function of Ω. The squares are obtained from the FDTD simulation of a rotating microdisk of $R = 590$ nm and $n = 3$ in free space, and the crosses from the stationary microdisk with the effective indices of refraction (inside and outside the disk) that include the rotation-induced changes. The dotted lines are linear fits showing that the Q changes exponentially with rotation speed.

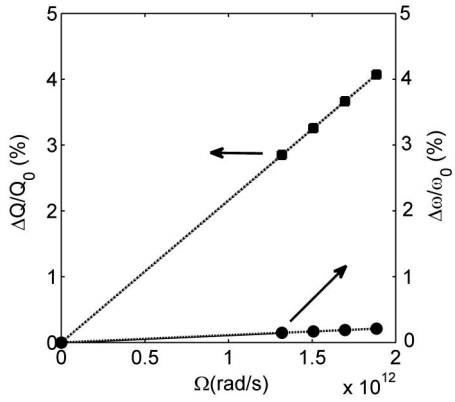

Fig. 4. Relative change in Q factor $\Delta Q/Q_0$ (squares) and the normalized frequency splitting $\Delta\omega/\omega_0$ (circles) as a function of the rotation speed Ω for the WG mode of $l = 1$, $m = -7$ in the dielectric microdisk of $R = 590$ nm and $n = 3$. The dotted lines are the linear fits. The slope of $\Delta Q/Q_0$ versus Ω is 2.16×10^{-12} and for $\Delta\omega/\omega_0$ is 1.12×10^{-13}.

the normalized frequency splitting $\Delta\omega/\omega_0$, where Q_0 and ω_0 are the Q factor and resonant frequency of the stationary cavity. Both scale linearly with Ω, and the slope for $\Delta Q/Q_0$ versus Ω is 2.16×10^{-12}, whereas the slope for $\Delta\omega/\omega_0$ versus Ω is 1.12×10^{-13}. The Q factor for this cavity is therefore ~20 times more sensitive to rotation than the resonant frequency. The Q not only determines the threshold pump level for lasing, but also affects the output power above the threshold. Thus the change of Q by rotation would modify the lasing thresholds for CW and CCW modes, and break the balance between the CW and CCW output power. The higher sensitivity of Q to Ω indicates the rotation-induced changes in lasing thresholds and output power can be more dramatic than the lasing frequency shift in the wavelength-scale microdisk lasers. Note that such high sensitivity results from the enhanced evanescent tunneling of light from the small disks, but it would reduce as the cavity grows in size.

We also investigate the dependence of $\Delta\omega/\omega_0$ and $\Delta Q/Q_0$ on the refractive index of the microdisk n_o^{disk}. Since the WG mode is tightly confined within the cavity by TIR from the disk boundary, the frequency splitting mostly depends on the change of the refractive index of the disk and not outside. The rotation-induced index change of the disk is $\Delta n = n_{\Omega}^{\text{disk}} - n_0^{\text{disk}} \approx (\frac{m\Omega}{n_0^{\text{disk}}\omega})$. The frequency splitting is proportional to Δn and therefore decreases with higher refractive index n_o^{disk} of the disk. The change in quality factor due to rotation, however, depends on the difference in refractive index inside and outside the disk. According to Eq. (23), index difference $|n_{\Omega}^{\text{disk}} - n_{\Omega}^{\text{outside}}|$ increases with n_o^{disk}, resulting in a larger change of Q.

As shown in Fig. 5, $\Delta Q/Q_0$ and $\Delta\omega/\omega_0$ display an opposite trend as n_o^{disk} varies, the former increases at larger n_o^{disk}, while the latter decreases. This result suggests that for the semiconductor microdisks with large refractive index, the rotation-induced change in quality factor is enhanced.

Finally we calculate the far field emission pattern from the rotating cavity and compare it to that from the stationary cavity. As shown in Fig. 6(b), rotation reduces the intensity modulation in the far field pattern [Fig. 6(a)]. A quantitative measure of the modulation depth is $\gamma = (I_{\max} - I_{\min})/(I_{\max} + I_{\min})$, where $I_{\max}$ ($I_{\min}$) is the

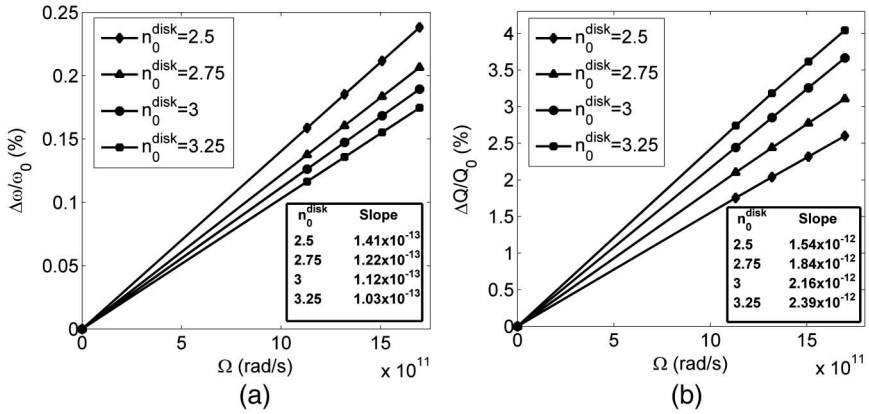

Fig. 5. (a) Normalized frequency splitting $\Delta\omega/\omega_0$ due to rotation for different refractive indices n_o^{disk} of the dielectric microdisk ($R = 590$ nm, $l = 1$, $m = \pm 7$). The lower inset shows the slopes from the linear fits for different n_o^{disk}; (b) The relative change of Q factor $\Delta Q/Q_0$ due to rotation for the CW mode ($m = -7$) for different refractive indices n_o^{disk} of the same disk. The lower inset shows the slopes from the linear fits for different n_o^{disk}.

maximal (minimal) field intensity. Figure 6 plots γ as a function of Ω. The decrease of γ is attributed to the unbalance between CW and CCW wave components in the resonant modes of the rotating cavity. To confirm this, we decompose the intracavity field distribution by the Bessel functions, $\Psi(r,\theta) = \sum_{m=-\infty}^{m=\infty} a_m J_m(nk_m r)e^{im\theta}$. As shown in Fig. 6(d), for a WG mode at $\Omega = 0$, the amplitude of the Bessel decomposition coefficients $|a_m|$ for $m = 7$ and -7 are equal and therefore the resonant mode form a standing wave along the azimuthal direction. When the cavity rotates, the resonant modes are no longer standing waves, but are travelling waves with either $m = 7$ or $m = -7$ as the dominant component, because the rotation allows differentiating between the CW and CCW waves and lifts their frequency degeneracy. This is illustrated in Fig. 6(e), for one particular mode of the rotating microdisk, $|a_{m=-7}|$ has much larger amplitude than $|a_{m=7}|$. As rotation speed increases, the ratio $|a_{m=7}|/|a_{m=-7}|$ keeps decreasing as shown in Fig. 6(f).

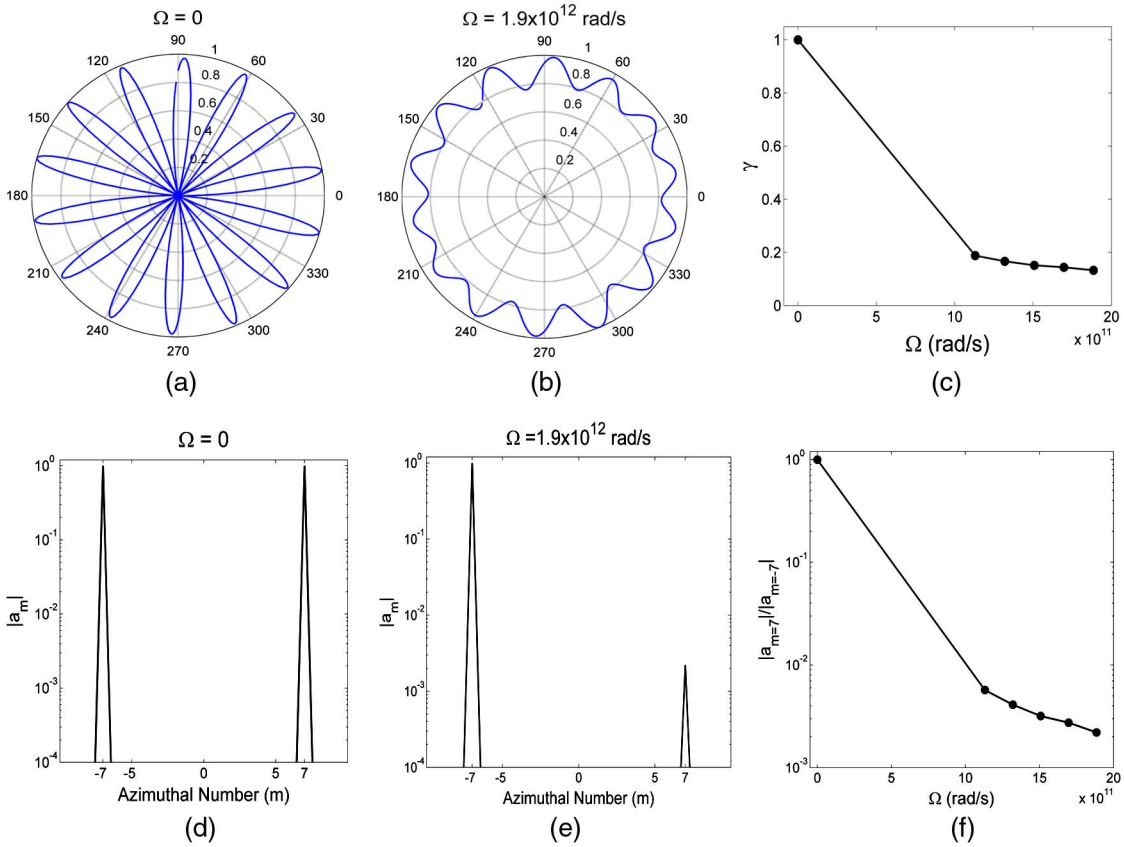

Fig. 6. (Color online) (a) Far field pattern for the WG mode of $l = 1$ and $m = \pm 7$ in the stationary microdisk of $R = 590$ nm and $n = 3$; (b) far field pattern of the same disk which rotates at $\Omega = 1.9 \times 10^{12}$ rad/s; (c) the far-field intensity modulation depth γ as a function of Ω; (d) Bessel decomposition of the intracavity field for the same mode as in (a); (e) Bessel decomposition of field inside the rotating cavity for the mode in (b); (f) ratio of the amplitudes of the Bessel coefficients as a function of Ω.

5. CONCLUSION

In summary, we developed a FDTD algorithm to simulate photonic structures in a rotating frame. The rotation angular velocity Ω is assumed to be constant in time, and the maximal speed $v = \Omega R$ to be small in magnitude compared to the speed of light so that any relativistic effect is negligible. Unlike the previous FDTD model which substitutes the constitutive relations into the Maxwell's equations and updates only E and H in time stepping, we calculate both E, H, and D, B by solving simultaneously and separately the Maxwell's equations (identical to that in a stationary frame) and the modified constitutive relations in the rotating frame. Excellent agreement between the FDTD simulations of the Sagnac effect in 2D closed cavities and the analytical results validates our model. For open cavities, UPML for stationary frame is adapted and the residual reflection from the UPML is shown to have negligible effects on the rotation-induced frequency shift and quality factor change of the wavelength-scale microdisk cavities as long as the maximal speed $v \ll c$. Our numerical results illustrate that the frequency splitting in an open microdisk cavity is larger than that in a closed cavity of same size. This is attributed to an increase of mode size in the open cavity. We have also calculated the change in quality factor and far-field emission pattern of the open cavities due to rotation. For wavelength-scale microdisk cavities, the relative change in quality factor by rotation is over an order of magnitude larger than that in resonant frequency, due to enhanced evanescent tunneling of light. Hence, monitoring the lasing threshold, the output power or the far-field emission pattern of a rotating microdisk laser can be a more sensitive technique for rotation sensing than detecting the beating frequency resulted by the Sagnac effect. The relative change of quality factor and resonant frequency due to rotation also depend on the refractive index of the microdisk, and they show an opposite trend: an increase in the refractive index of the stationary disk enhances the Q change by rotation but reduces the frequency splitting.

As the cavity size approaches the wavelength, the sensitivity of the total-internal-reflection based microdisk laser becomes comparable to that of a circular Bragg microlaser. The advantages of the microdisk over the Bragg resonator are the small footprint and easiness of fabrication. Finally, we note that the FDTD algorithm developed here can be applied to any complex photonic structures in the rotating frame, although it is applied to dielectric microdisks in the current work. It can be extended to 3D systems, facilitating design and optimization of optical gyroscopes based on novel photonic structures.

ACKNOWLEDGMENTS

We thank Dr. Vincent Moncrief of Physics Department, Yale University, for discussions related to Maxwell's equations in a rotating frame. This work is supported partly by the National Science Foundation (NSF) under Grant Nos. ECCS1068642 and ECCS1128542.

REFERENCES

1. C. Ciminelli, F. Dell'Olio, C. E. Campanella, and M. N. Armenise, "Photonic technologies for angular velocity sensing," Adv. Opt. Photon. **2**, 370–404 (2010).
2. B. Z. Steinberg, "Rotating photonic crystals: a medium for compact optical gyroscopes," Phys. Rev. E **71**, 056621 (2005).
3. B. Z. Steinberg and A. Boag, "Propagation in photonic crystal coupled-cavity waveguides with discontinuities in their optical properties," J. Opt. Soc. Am. B **23**, 1442–1450 (2006).
4. A. B. Matsko, A. A. Savchenkov, V. S. Ilchenko, and L. Maleki, "Optical gyroscope with whispering gallery mode optical cavities," Opt. Commun. **233**, 107–112 (2004).
5. J. Scheuer and A. Yariv, "Sagnac effect in coupled resonator slow light waveguide structures," Phys. Rev. Lett. **96**, 053901 (2006).
6. C. Peng, Z. Li, and A. Xu, "Optical gyroscope based on a coupled resonator with the all-optical analogous property of electromagnetically induced transparency," Opt. Express **15**, 3864–3875 (2007).
7. C. Sorrentino, J. R. E. Toland, and C. P. Search, "Ultra-sensitive chip scale Sagnac gyroscope based on periodically modulated coupling of a coupled resonator optical waveguide," Opt. Express **20**, 354–363 (2012).
8. R. Novitski, B. Z. Steinberg, and J. Scheuer, "Losses in rotating degenerate cavities and a coupled-resonator optical-waveguide rotation sensor," Phys. Rev. A **85**, 023813 (2012).
9. B. Z. Steinberg, J. Scheuer, and A. Boag, "Rotation-induced superstructure in slow-light waveguides with mode-degeneracy: optical gyroscopes with exponential sensitivity," J. Opt. Soc. Am. B **24**, 1216–1224 (2007).
10. S. Sunada and T. Harayama, "Sagnac effect in resonant microcavities," Phys. Rev. A **74**, 021801(R) (2006).
11. T. Harayama, S. Sunada, and T. Miyasaka, "Wave chaos in rotating optical cavities," Phys. Rev. E **76**, 016212 (2007).
12. S. Sunada and T. Harayama, "Design of resonant microcavities: application to optical gyroscopes," Opt. Express **15**, 16245–16254 (2007).
13. J. Scheuer, "Direct rotation-induced intensity modulation in circular Bragg micro-lasers," Opt. Express **15**, 15053–15059 (2007).
14. M. Skorobogatiy and J. D. Joannopoulos, "Rigid vibrations of a photonic crystal and induced interband transitions," Phys. Rev. B **61**, 5293 (2000).
15. M. Skorobogatiy and J. D. Joannopoulos, "Photon modes in photonic crystals undergoing rigid vibrations and rotations," Phys. Rev. B **61**, 15554 (2000).
16. B. Z. Steinberg, "Two-Dimensional Green's function theory for the electrodynamics of a rotating medium," Phys. Rev. E **74**, 016608 (2006).
17. C. Peng, R. Hui, X. Luo, Z. Li, and A. Xu, "Finite-difference time-domain algorithm for modeling Sagnac effect in rotating optical elements," Opt. Express **16**, 5227–5240 (2008).
18. T. Shiozawa, "Phenomenological and electron-theoretical study of the electrodynamics of rotating systems," Proc. IEEE **61**, 1694–1702 (1973).
19. A. Taflove, *Computational Electrodynamics: The Finite-Difference Time-Domain Method* (Artech House, 1995).